Modeling of Reoxidation Inclusion Formation During Filling of Steel Castings

Kent D. Carlson and Christoph Beckermann

Department of Mechanical and Industrial Engineering

The University of Iowa, Iowa City, IA 52242

Abstract

A reoxidation inclusion model is being developed that simulates the entire life cycle of inclusions during the filling of steel castings. There are two ways that inclusions can be introduced into the casting: inclusions can be released at the inlet to model tiny deoxidation or other larger inclusions entering the mold cavity from the ladle, and they can also be born on the metal free surface, where contact with oxygen from the atmosphere creates them. These models can be used separately or together. Inclusion motion is calculated by solving an equation of motion for each inclusion at each time step. The growth of reoxidation inclusions is modeled both by oxide growth due to oxygen pickup at the free surface as well as by inclusion agglomeration (combination) when inclusions come close enough together to merge. All of these pieces of the inclusion model have been implemented in commercial casting simulation software, and an application is provided to qualitatively compare the simulation results to experimental results. A parametric study is also performed, to examine the effect of various values specified in the model. Once completed, the present simulation model will provide a tool for foundries to determine the final location and characteristics of reoxidation inclusions in steel castings.

1. Introduction

The removal of oxide inclusions from castings and the subsequent repair of those castings are expensive and time consuming procedures. Svoboda et al.[1] estimated that twenty percent of the cost of producing castings is due to the removal of inclusions and the repair of the resulting defect areas with weld metal. Inclusions that remain in the casting adversely affect machining and mechanical performance, and may cause the casting to be rejected for failing to meet the radiographic standard requirements specified by the customer regarding allowable inclusion severity. Reoxidation inclusions, which form when deoxidized steel comes into contact with oxygen during mold filling, make up a substantial portion of the inclusions found in steel castings. Griffin and Bates[2] estimated that 83% of the macro-inclusions found in low-alloy steel castings are reoxidation inclusions, as are 48% of those found in high-alloy steel castings. The primary source of oxygen in reoxidation inclusion formation is air, which contacts the metal stream during pouring and the metal free surface in the mold cavity during filling (see Figure 1).

At present, trial-and-error and experience are the only tools that foundry engineers have at their disposal to solve inclusion problems in steel castings. If a casting has inclusion problems, the foundry engineer may change the pouring practice or gating design for the casting in hopes that this will eliminate or reduce the severity of the problem. Changing the pouring or gating will change melt flow patterns during filling. This may reduce the amount of reoxidation inclusions created, or it may merely change the final location of macro-inclusions; if the inclusions are swept into a riser rather than collecting on the cope surface of the casting, the inclusion problem is solved even if the volume of reoxidation inclusions created does not change. In order to avoid inclusion problems or to reduce their severity, foundries often employ special gating techniques to reduce the contact area and time between the melt and the atmosphere during mold filling or to trap inclusions inside the runners. However, while a poor gating system can create inclusion problems in castings, a good gating system will not necessarily prevent inclusion problems. Thus, several iterations on the rigging of a casting may be necessary to resolve inclusion issues.

In an attempt to provide foundry engineers with a tool for eliminating or minimizing inclusion problems, a model is being developed that simulates the formation, growth, and motion of reoxidation inclusions during the pouring of steel castings. This model, which is being developed within the commercial casting simulation software MAGMASOFT[3], will allow foundries to predict the final location, size, number and other characteristics of reoxidation inclusions in a casting. This information can be used to help determine whether or not a given mold design will lead to inclusion problems, without having to expend the time, effort and money to produce the casting to determine this information.

The various components of the inclusion model that are currently implemented in MAGMASOFT are described in Section 2. A preliminary application of this model to perform a parametric study and to compare simulation results with experimental results is presented in Section 3. Ongoing work is then summarized in Section 4. It is stressed that the work on inclusion modeling is well underway, but is not yet complete. This paper is intended to serve as a status report, showing some very promising preliminary results.

2. Modeling Inclusion Formation, Growth, Agglomeration, and Motion

This section describes the different aspects of inclusion modeling currently implemented in MAGMASOFT. These aspects include inclusion formation, growth, agglomeration and motion. Presently, inclusions can be modeled either as spheres or as thin disks (i.e., pancake-shaped inclusions), as shown in Figure 2. Spheres are characterized by a diameter d, while disks are characterized by a disk diameter d_{disk} and thickness t.

<u>Formation</u>

The present model provides two mechanisms that can be used to create reoxidation inclusions: release and birth (nucleation). These mechanisms can be used separately or together.

Release: The release mechanism allows the user to release inclusions at the inlet to the mold. This option can be used to model tiny deoxidation or other larger inclusions that enter from the ladle into the casting cavity with the melt during pouring. This way, the effects of the cleanliness of the melt from the ladle can be examined. The user chooses the initial size of the inclusions that are released by specifying d_0 (cm) for spheres or $d_{disk,0}$ and t_0 (both in cm) for disks. The user also specifies a "release" spacing, l_{rel} (cm), and the model releases inclusions spaced l_{rel} apart over the inlet area. Each inclusion is assigned an initial velocity equal to that of the liquid metal at the release location. The model then determines the inclusion release frequency, f_{rel} (s^{-1}), from

$$f_{rel} = \vec{v}_{in} / l_{rel} \tag{1}$$

where $\vec{v}_{in}$ (cm/s) is the average inlet velocity, and releases inclusions at time intervals of $1/f_{rel}$ seconds. This provides a continuous release of inclusions with an inclusion number density, n_{rel} (cm^{-3}), of

$$n_{rel} = l_{rel}^{-3} \tag{2}$$

If the approximate inclusion number density in the melt coming from the ladle is known, this can be used as n_{rel} to determine l_{rel} from Equation (2); i.e., $l_{rel} = n_{rel}^{-1/3}$.

Birth: The birth mechanism creates tiny new inclusions on the free surface of the melt during filling. The phenomenon of nucleation of oxide inclusions on a low-carbon aluminum-killed (LCAK) liquid steel free surface has been photographed by Wang et al.[4] This series of photographs is reproduced in Figure 3. It can be seen that the free surface is initially free of inclusions (Figures 3a and 3b). The inclusions nucleate at approximately the time of the photograph in Figure 3c. The initial inclusion spacing appears to be around 10 microns. The later photographs show continued growth and agglomeration of the inclusions, as discussed in more detail below.

In the present birth model, the initial size of the inclusions that nucleate on the free surface is assumed to be negligibly small. In practice, a small but finite value for the initial diameter is used, such that the initial inclusion volume is still negligibly small. The user specifies a "nucleation" spacing, l_0 (cm), which indicates the desired initial spacing between inclusions that

nucleate on the free surface. This value would typically be different from the release spacing, l_{rel}. The nucleation spacing can be related to the number of nuclei per unit free surface area, n_0'' (cm^{-2}), by the equation

$$n_0'' = l_0^{-2} \tag{3}$$

In order to compute the area of the free surface that is available for nucleation of new inclusions, the following approximations are made. The total area of the free surface in a computational cell, $A_{FS,cell}$ (cm^2), is first approximated using the equation

$$A_{FS,cell} = 4VOF(1-VOF)f_{sr} \times 1.2(dx \times dy \times dz)^{2/3} \tag{4}$$

where VOF is the volume of fluid [VOF = (volume of fluid in cell)/(total cell volume), $0 \leq VOF \leq 1$]; f_{sr} is a surface roughness factor that accounts for the fact that fluid flow simulations cannot capture the actual roughness of the metal surface (see, for example, the picture on the left side of Figure 1); and dx, dy and dz (all in cm) are the flow cell dimensions. The term $4VOF(1-VOF)$ in Equation (4) determines the size of the free surface based on how much liquid metal the flow cell contains. This term has a maximum value of one when the cell is half full (i.e., VOF = 0.5), and a minimum value of zero when the cell is either completely empty or completely full (i.e., VOF = 0 or VOF = 1). The term $1.2(dx \times dy \times dz)^{2/3}$ in Equation (4) approximates the area of the free surface, assuming the cell is half full. To understand this, consider the schematics shown in Figure 4. Figure 4a shows a general free surface, while Figures 4b and 4c show free surfaces for a uniform grid cell (i.e., $dx = dy = dz$). If the grid is uniform, the term $1.2(dx \times dy \times dz)^{2/3}$ simplifies to $1.2dx^2$, which is the area shown in Figure 4b multiplied by 1.2. The factor 1.2 is used because the actual orientation of the free surface within a cell is unknown. The minimum possible area for a half-full cell is the surface shown in Figure 4b, which has an area of $1.0dx^2$. The maximum area, shown in Figure 4c, is $1.41dx^2$. The factor 1.2 is used because it is the average of the minimum and maximum values. While the above method for computing the area of the free surface within in a computational cell may appear to be crude, more exact calculations cannot be justified in view of the fact that typical filling simulations are far from being able to resolve all details of the highly turbulent free surface that can exist during filling of a steel casting.

Once the total free surface area in a cell is computed, the number density of the inclusions already existing on that free surface area, n_{exist}'' (cm^{-2}), can be found from

$$n_{exist}'' = N_{exist}/A_{FS,cell} \tag{5}$$

where N_{exist} is the number of inclusions that already exist in the flow cell that contains a free surface. Here, it is assumed that all inclusions within a free surface cell are on the free surface. From this value, the spacing of the existing inclusions, l_{exist} (cm), can be approximated as

$$l_{exist} = (n_{exist}'')^{-1/2} \tag{6}$$

If the spacing between existing inclusions exceeds the user-specified nucleation spacing, l_0, then inclusion birth may occur, provided there is available free surface area. The free surface area available for inclusion birth, A_{birth} (cm^2), is calculated from

$$A_{birth} = A_{FS,cell} - A_{exist} \tag{7}$$

where A_{exist} (cm^2) is the sum of the cross-sectional areas of all existing inclusions in this cell

$$A_{exist} = \sum_{j=1}^{n} \frac{\pi}{4} d_j^2 \tag{8}$$

where d_j is the diameter of inclusion j (d for spherical inclusions and d_{disk} for disk-shaped inclusions), and n is the total number of existing inclusions in this cell.

If A_{birth} calculated from Equation (7) is greater than zero, birth will occur. The number of inclusions that will be created, N_{birth}, is determined from

$$N_{birth} = n_0'' A_{birth} = l_0^{-2} A_{birth} \tag{9}$$

This value is then rounded up to the nearest integer, and N_{birth} inclusions are added to the cell that contains a free surface, spaced a distance of l_0 apart.

In practice, l_0 should be chosen smaller than the smallest grid dimension (dx, dy, or dz), in order to ensure that there is at least one inclusion in each cell that contains a free surface. On the other hand, specifying a nucleation spacing that is comparable to the one observed in experiments (see Figure 3), i.e., about 10 microns, would result in a total number of inclusions that is too large for present-day computing resources. Hence, a compromise must be found that provides final results that are reasonably independent of the number of inclusions generated by the above birth model and that can be obtained within present computational capabilities. This issue is examined in detail in Section 3.

Growth

When reoxidation inclusions are on the melt free surface, they will absorb oxygen from the atmosphere and grow as a result. This phenomenon is governed by the equation

$$\frac{\partial (\rho_{incl} V_{incl})}{\partial t} = \rho_{incl} A_{FS,incl} \beta \tag{10}$$

In this equation, β is an effective, overall mass transfer coefficient (cm/s); ρ_{incl} and V_{incl} are the inclusion density (kg/cm^3) and volume (cm^3), respectively; and $A_{FS,incl}$ is the area (cm^2) of the melt free surface that is contributing oxide to the growing inclusion. The model currently assumes that the mass transfer coefficient β is a constant; however, one of the next model enhancements will be to model this coefficient as a variable that accounts for variations in the oxidation rate due to changes in the flow conditions. The present version of the model also assumes that the inclusion density is a constant.

In the present growth model, the total oxidation rate is proportional to the entire free surface area at any instant of time. However, the amount of oxide formed during a given time step must be apportioned to the individual inclusions. This can be done in a cell-by-cell manner, since each free surface cell has at least one inclusion. The present apportioning procedure is based on the idea that larger inclusions "attract" oxide from a larger portion of the free surface than smaller inclusions do. Hence, in order to determine the area $A_{FS,incl}$ in Equation (10) it is assumed that the total flow cell free surface area [$A_{FS,cell}$, defined in Equation (4)] is divided among the inclusions within that flow cell, proportional to each inclusion's surface area. This can expressed as,

$$A_{FS,incl} = \frac{SA_{incl}}{\sum\limits_{j=1}^{n} SA_{incl,j}} A_{FS,cell} \tag{11}$$

where n represents the number of inclusions in the flow cell. The surface area of spherical inclusions is

$$SA_{sphere} = \pi d^2 \tag{12}$$

while the surface area of disk-shaped inclusions is

$$SA_{disk} = \frac{\pi}{2} d_{disk}^2 + \pi d_{disk} t \tag{13}$$

However, note that for thin disks such as the one shown in Figure 2b, the surface area on the disk faces (i.e., the top and bottom surfaces) is much larger than the area created by the thickness [given by the term $\pi d_{disk} t$ on the right side of Equation (13)]. Because the first term on the right side of Equation (13) is much larger than the second, the second term can be neglected. If this is done, then substituting either Equation (12) or (13) into Equation (11) results in

$$A_{FS,incl} = \frac{d_{incl}^2}{\sum\limits_{j=1}^{n} d_{incl,j}^2} A_{FS,cell} \tag{14}$$

where d_{incl} is d for spherical inclusions, and d_{disk} for disk-shaped inclusions.

With the above information, the volume of each inclusion after growth, V_{incl}, can be calculated from Equation (10). This new volume is then used to compute the new inclusion size. For spheres, the diameter after growth is given by the equation relating the volume of a sphere to its diameter

$$d = \left(6V_{incl}/\pi\right)^{1/3} \tag{15}$$

For disks, the volume is related to the diameter and thickness by

$$V_{incl} = \frac{\pi}{4} d_{disk}^2 t \tag{16}$$

Note that growth can cause an increase in both the diameter and the thickness. An assumption must be made in order to determine both of these quantities from the volume after growth. The assumption used in the model is that the thickness and diameter both grow by the same ratio, r_{grow}. In other words, the disk diameter and thickness after growth can be written as

$$d_{disk} = r_{grow} d_{disk,old} \tag{17}$$

and

$$t = r_{grow} t_{old} \tag{18}$$

where $d_{disk,old}$ and t_{old} are the values before growth. Substituting Equations (17) and (18) into Equation (16) results in

$$V_{incl} = \frac{\pi}{4} r_{grow}^3 d_{disk,old}^2 t_{old} \tag{19}$$

Equation (19) can be solved for r_{grow}, and then the disk diameter and thickness after growth can be calculated from Equations (17) and (18).

Agglomeration

Aside from growth, inclusions can also increase in size during filling by colliding with and sticking to each other, to form a single larger inclusion. This is known as agglomeration. While this can happen anywhere in the melt due to random collisions, it is more likely to occur on the liquid metal free surface. This is because solid inclusions on the liquid free surface cause small indentations in the free surface. These indentations extend beyond the inclusions themselves, and essentially create an effect not unlike gravity over very small distances (on the order of ten to a few hundred microns). To understand this, imagine placing two bowling balls on a trampoline. If the balls get close enough, the indentations they each make in the trampoline will interact, and the balls will roll together and touch. This can be seen in Figure 5, which shows photographs of inclusions agglomerating on the free surface of low-carbon aluminum-killed (LCAK) liquid steel. These photos, presented by Shibata et al.[5], are clear evidence of the attractive forces between inclusions that were essentially motionless relative to each other in the first frame of Figure 5. The photographs obtained by Wang et al.[4] and reproduced in Figure 3 also show the phenomena of growth and agglomeration on a LCAK steel free surface. The inclusions that nucleated on the liquid steel surface (Figure 3d) grow until their spacing becomes small enough that they agglomerate (Figures 3e and 3f).

The present agglomeration model is shown schematically in Figure 6, for both spheres and disks. If two inclusions are within some critical distance L_1 of each other, they are assumed to agglomerate immediately. The assumption of instantaneous agglomeration neglects the inertia and drag forces on the particles during agglomeration; it is needed because of the difficulty to resolve the motion of the inclusions over the small distances involved in the agglomeration process. To determine if two inclusions agglomerate, it is necessary to determine the critical distance L_1 shown in Figure 6. This was done using the experimental data of Shibata et al.[5], shown in Figure 7. They measured accelerations and separation distances of inclusions such as those shown in Figure 5 to determine the attractive forces and critical distances ("acting length" in Figure 7) between inclusions. The data shown in Figure 7 indicates that the critical distance

depends primarily on the radius of the larger of the two inclusions. This can be understood by returning to the bowling ball analogy. Assuming that the bowling balls have the same density, a larger bowling ball would create a larger indentation in the trampoline. The size of the smaller bowling ball becomes less important, because it will be attracted to the larger bowling ball as soon as it encounters the larger indentation caused by the larger ball. To determine the relationship between the radius of the larger inclusion and the critical distance, a line was drawn through the center of the data shown in the upper part of Figure 7. The equation of this line is approximately given by

$$L_1 (\text{cm}) = 0.084 \sqrt{d_{\max} / 2} \qquad (20)$$

where $d_{\max}$ (cm) is the diameter of the larger of the two inclusions. For simplicity, the same relation is used for disks, replacing $d_{\max}$ with $d_{disk,\max}$. It is important that the diameter used in Equation (20) is in centimeters, because the constant in front of the square root has units of $(\text{cm})^{1/2}$. Note that the critical distance given in Equation (20) is only valid if both inclusions involved are on the metal free surface. If one or both are immersed in the metal, the attractive surface force is absent, and a critical distance of $L_1 = 0$ is used. Finally, note that more than two inclusions can be involved in an agglomeration. It is possible for several inclusions to be located on the free surface close enough to a given inclusion to satisfy the agglomeration criterion, in which case all inclusions within this distance are combined.

When inclusions agglomerate, it is necessary to determine the properties of the newly formed inclusion. This is done by first summing the masses and volumes of the inclusions involved, to determine the mass and volume of the agglomerated group, m_{agg} (kg) and V_{agg} (cm^3), respectively. The density of the newly agglomerated inclusion, ρ_{agg} (kg/cm^3), is then found from

$$\rho_{agg} = m_{agg} / V_{agg} \qquad (21)$$

Since the densities of the inclusions are currently assumed to be equal and constant, the above equation simply gives $\rho_{agg} = \rho_{incl}$. For spheres, the diameter of the new inclusion, d_{agg} (cm), is determined from

$$d_{agg} = \left(6V_{agg} / \pi \right)^{1/3} \qquad (22)$$

For disks, both the diameter and the thickness of the new inclusion must be determined from the agglomerated volume. To do this, the model assumes that the new inclusion thickness, t_{agg} (cm), is equal to the maximum thickness value of all inclusions involved in the agglomeration, i.e., $t_{agg} = \text{MAX}(t)$. The new agglomerated disk diameter, $d_{disk,agg}$ (cm), is then found from

$$d_{disk,agg} = \sqrt{\frac{4V_{agg}}{\pi t_{agg}}} \qquad (23)$$

The location of the new inclusion, $\vec{x}_{agg}$ (cm), is given by the center of mass of the inclusions that were involved in the agglomeration, which can be written as

8

$$\vec{x}_{agg} = \sum_{j=1}^{n} m_j \vec{x}_j \bigg/ \sum_{j=1}^{n} m_j \qquad (24)$$

where $\vec{x}_j$ and m_j are the position vector and mass of inclusion j, respectively, and n is the number of inclusions that agglomerated. Finally, the velocity of the new inclusion, $\vec{v}_{agg}$ (cm/s), is determined by conservation of linear momentum for the group of inclusions involved. This is expressed as

$$\vec{v}_{agg} = \sum_{j=1}^{n} m_j \vec{v}_j \bigg/ \sum_{j=1}^{n} m_j \qquad (25)$$

where $\vec{v}_j$ is the velocity vector of inclusion j.

Motion

In order to determine the final location of inclusions, it is necessary to track their movement from the time they form until filling is complete. In the present model, this is done by solving the following equation of motion for each inclusion, at each time step:

$$m_{incl} \frac{d\vec{v}_{incl}}{dt} = F_{drag} + F_{buoyancy} \qquad (26)$$

where m_{incl} and $\vec{v}_{incl}$ are the mass (kg) and velocity (cm/s) of the inclusion, respectively; and F_{drag} and $F_{buoyancy}$ are the drag and buoyancy forces (kg-cm/s^2) acting on the inclusion. Since agglomeration of inclusions is assumed to be instantaneous (see the previous sub-section), no attraction forces between inclusions are included in the above equation. Other forces (virtual mass, lift, drag due to the presence of other inclusions, etc.) are also neglected. In addition, Equation (26) assumes that the inclusion mass is constant during motion. If the inclusions are assumed to be spherical, Equation (26) can be expressed as

$$\rho_{incl} \frac{d\vec{v}_{incl}}{dt} = \frac{18\mu_l}{d_{incl}^2} \left(\vec{v}_l - \vec{v}_{incl}\right)\left(1 + 0.15\,\mathrm{Re}^{0.687}\right) + \left(\rho_{incl} - \rho_l\right)\vec{g} \qquad (27)$$

where ρ_{incl} and d_{incl} are the density (kg/cm^3) and diameter (cm) of the inclusion, respectively; ρ_l and μ_l are the density (kg/cm^3) and dynamic viscosity (kg/cm-s) of the liquid, respectively; $\vec{g}$ is the gravity vector (cm/s^2); t is the time (not the disk thickness); and Re is the Reynolds number, which is a dimensionless number defined in terms of the difference between the velocity of the inclusion ($\vec{v}_{incl}$) and the velocity of the surrounding liquid metal ($\vec{v}_l$) as

$$\mathrm{Re} = \frac{\left|\vec{v}_l - \vec{v}_{incl}\right|\rho_l d_{incl}}{\mu_l} \qquad (28)$$

The first term on the right side of Equation (27) is the drag force, and the second term is the buoyancy force. The drag force is written in terms of a dimensionless drag coefficient, C_D, given by

$$C_D = \frac{24}{\mathrm{Re}}\left(1 + 0.15\,\mathrm{Re}^{0.687}\right) \tag{29}$$

This drag coefficient correlation is valid for $\mathrm{Re} \leq 1000$.

During each time step of the filling simulation, Equation (27) is solved for each inclusion to determine its velocity. This information is then used to update the location of each inclusion according to $d\vec{x}_{incl}/dt = \vec{v}_{incl}$, where $\vec{x}_{incl}$ is the position vector of an inclusion. If an inclusion comes into contact with a mold wall, it is assumed to stick to the wall.

Note that the inclusion momentum equation given in Equation (27) is employed even when disk-shaped inclusions are used. To account for the size and shape of each disk in the momentum equation, a volume equivalent diameter is used in Equation (27). This is the diameter that the disk would have, based on its volume, if it were spherical. The volume equivalent diameter, d_{eq} (cm), is determined from

$$d_{eq} = \sqrt[3]{\frac{3}{2}d_{disk}^2\,t} \tag{30}$$

After the equation of motion has been solved for each inclusion, the volume equivalent diameter is converted back into a disk diameter with the equation

$$d_{disk} = \sqrt{\frac{2}{3}\frac{d_{eq}^3}{t}} \tag{31}$$

3. Application of the Model

As mentioned earlier, the model described in the previous section has been implemented in the casting simulation software MAGMASOFT. This section describes the results of a parametric study that was performed with this software to evaluate the current state of the model.

The geometry used in this study is the plate geometry shown in the upper left of Figure 8. The plate is 1 in. thick by 10 in. wide by 12 in. long, with a 4 in. diameter by 4 in. high end riser. This particular geometry was selected because it was used for a separate experimental study of inclusion formation, so there is experimental data with which to compare simulation results. Filling of this geometry is simulated for 1022 steel in a furan sand mold. The pouring temperature is 1581°C (2878°F), which gives a superheat of 80°C (144°F). The pouring time is 7 seconds.

The present investigation focuses on the birth model, so this model is used in all cases presented in this work. The release model is not employed in any of the simulations discussed here. The inclusion density is taken to be constant and equal to 0.003 kg/cm³; this is approximately the density of the alumina inclusions that are prevalent in reoxidation. The inclusion size at birth is specified as $d = 4$ microns for spherical inclusions, and $d_{disk} = 4$ microns, $t = 2$ microns for disk-shaped inclusions. This size is small enough that it results in an essentially negligible initial inclusion volume at birth. The mass transfer coefficient for these simulations is specified as $\beta = 0.0002$ cm/s; this value simply provides a reasonable growth rate

for the purpose of the present simulations. As mentioned before, an improved oxidation rate model will be included in the near future.

Other simulation parameters that must be specified include the grid size (or number of metal cells); the nucleation spacing, l_0; the surface roughness factor, f_{sr}; and whether to use spherical or disk-shaped inclusions. These parameters were varied to create the present parametric study. The values of these parameters for the five cases considered are listed in Table 1.

The simulated inclusions at 10% increments during filling are shown for Case 1 in Figure 8. As the plate becomes nearly filled, a group of relatively large inclusions are seen to form and stick to the middle of the plate cope surface. This is caused by a swirling behavior of the liquid metal in this region when the plate is nearly filled. The swirling of the liquid metal brings many inclusions into the same area, where they agglomerate on the free surface to form the large inclusions seen on the plate cope surface in Figure 8. However, Figure 8 also shows that smaller inclusions (around 100 microns in diameter) are evenly distributed throughout the casting. A top view of the inclusions at the end of filling is shown in Figure 9a. This simulation result can be compared to the two experimental plates shown in Figure 9b. These plates were cast with the rigging shown in Figure 8, and then ⅛ in. of material was machined from their cope surfaces. The circles drawn on the plates in Figure 9b are inclusion counts, where 1-in. diameter circles are drawn around all visible inclusions on the machined cope surfaces. Note that the locations of the inclusions seen in the experimental plates in Figure 9b are in good agreement with the locations of the largest inclusions shown in Figure 9a. The final inclusion plots produced for Cases 2 – 5 look qualitatively very similar to those of Case 1 in Figures 8 and 9; therefore, they are not shown here. It is interesting to note, however, that even as the model parameters are varied, the simulated final locations of the largest inclusions match the experimental results.

Table 1 summarizes the results of the parametric study mentioned above. Furthermore, the final size and volume distributions of the inclusions for each case are presented in Figures 10 – 14. Figures 10a – 14a show the distribution of the number of inclusions for each case. Final inclusion diameter is plotted on the x-axis of these figures. The inclusions were grouped by their diameters into one-micron diameter increments and counted. This count (i.e., the number of inclusions in each one-micron interval) was then divided by the total number of inclusions at the end of the simulation and plotted on the y-axis, as the number fraction of inclusions per micron of diameter. Hence, the area under each of the curves in Figures 10a – 14a is equal to unity. These figures show the distribution of inclusions, based on their diameter. For example, Figure 10a shows that the majority of inclusions produced in this simulation have a final diameter of around 100 microns, with very few inclusions larger than 500 microns (0.5 mm). Figures 10b – 14b show the distribution of the final inclusion volume as a function of inclusion diameter. These figures also plot the final inclusion diameter on the x-axis, but now the total volume of the inclusions within each micron increment of diameter are computed and divided by the total volume of all inclusions. This is plotted on the y-axis, as the total final volume fraction per micron of diameter. The area under each of the curves in Figures 10b – 14b is also equal to unity. These figures relate the distribution of the total inclusion volume to the inclusion diameter. For example, Figure 10b shows that the majority of the final inclusion volume consists of inclusions 500 microns or smaller, with a peak around 200 microns. The presence of relatively few large inclusions can be clearly observed in Figures 10b – 14b.

As shown in Table 1, Case 1 used a grid with about 26,000 metal cells (i.e., cells that will contain metal at the end of filling), a nucleation spacing of 0.5 cm, a surface roughness factor of 1, and spherical inclusions. This simulation resulted in a final total inclusion volume of 0.276 cm^3, consisting of about 147,000 inclusions, with a maximum inclusion diameter of 0.269 cm (2.69 mm). A total of about 213,000 inclusions were generated, implying that about 66,000 inclusions combined together through agglomeration. Case 2 used all the same parameters as Case 1, except that the nucleation spacing was reduced from 0.5 cm to 0.25 cm. Table 1 shows that in Case 2 the smaller nucleation spacing resulted in a final count of about 284,000 inclusions, which is nearly twice as many inclusions as in Case 1. As in Case 1, Case 2 resulted in a final total inclusion volume of 0.276 cm^3. This shows that the total volume of oxide generated is not affected by the number of inclusions simulated. The average inclusion diameter is different for the two cases (Table 1), since the same total inclusion volume is produced with a different number of inclusions. However, Table 1 shows that, despite the vastly different number of inclusions generated in Cases 1 and 2, the final diameter of the largest inclusion is approximately the same. Comparing Figures 10a and 11a, it is seen that the normalized size distribution of the final inclusions is also very similar in both cases. The peaks in both figures are of the same magnitude and occur at diameters slightly under 100 microns. This indicates that the predicted final size distribution of the inclusions is not affected by the number of the inclusions simulated, if the size distribution is normalized by the total final number of inclusions. This result is important for trying to minimize the number of inclusions in a simulation in order to reduce computational times. The volume distributions for Cases 1 and 2 are also quite similar (Figures 10b and 11b). In particular, the presence of a few inclusions of a large volume is predicted in approximately the same manner in both cases. This implies that the prediction of the large inclusions is not strongly affected by the total number of inclusions simulated. Since the large inclusions are of primary concern to steel foundries, this finding again can be used to minimize the number of inclusions in a simulation. Although the curves are of a similar shape, note that the magnitude of the peak just below 200 microns is about 0.0038/micron in Figure 10b, while it is about 0.0048/micron in Figure 11b. This indicates that more of the oxide volume is distributed among the smaller inclusions in Case 2 than in Case 1, which can be attributed to the much larger total number of inclusions in Case 2 than in Case 1.

Case 3 provides a check for grid independence: this case uses the same parameters as Case 2, except that it uses a grid that has about half the number of metal cells used in Case 2 (about 13,000). The total inclusion volume resulting for Case 3 is 0.279 cm^3, a value very close to the first two cases. Case 3 results in about 219,000 inclusions, which is a somewhat smaller number than in Case 2. However, both the maximum and average inclusion diameters in Case 3 are similar to Case 2. Comparing Figures 11a and 12a, it is seen that the normalized distribution of inclusions over the range of diameters is very similar. The peak value in Case 3 occurs at about the same diameter as in Case 2, although the fraction of inclusions at the peak is about 10% smaller. Comparing Figures 11b and 12b, the trends are also very similar. Again, the peak volume fraction in Figure 12b is somewhat lower than in Figure 11b. This indicates that more of the volume in Case 3 comes from somewhat larger inclusions, which can be seen by comparing these figures in the range of about 700 to 1300 microns (0.7 – 1.3 mm). The similarity of the results from Cases 2 and 3 gives some confidence in the grid independence of the present inclusion formation model. It should be noted that the similarity between the results from Cases 2 and 3 also implies a degree of time step independence, because the time step was larger in Case 3 than in Case 2. The time step in MAGMASOFT is variable and automatically determined

based on many factors, one of which is grid size. Coarser grids lead MAGMASOFT to use larger time steps.

Case 4 is the same as Case 1, except that the inclusions are modeled as disks rather than spheres. This case produces a final inclusion volume of 0.276 cm³, which is the same as in Case 1. The final number of inclusions in Case 4 (135,000) is also similar to Case 1. As expected, the maximum diameter is very different: the maximum disk diameter in Case 4 is nearly 1 cm, while the largest sphere diameter in Case 1 is only 0.27 cm. Rather than growing uniformly in all directions, the disk diameter increases much more than the thickness. This can be seen by noting that the initial ratio of d_{disk}/t is 2, while the final maximum ratio is 39. Since the growth model increases both the diameter and thickness by the same ratio, this indicates that the largest inclusion underwent many agglomerations, since in agglomeration the thickness is taken as the maximum value of the inclusions involved. Indeed, the largest inclusion in this simulation actually contains about 1,760 agglomerated inclusions. Comparing Figures 10 and 13, notice again that they are qualitatively very similar, except the x-axis scale is different due to the larger range of disk diameters. If one would scale the horizontal axes in Figures 10 and 13 by the largest inclusion diameters, the distributions would more directly coincide.

Finally, Case 5 is the same as Case 1, except a surface roughness factor, f_{sr}, of 10 (rather than 1) is used. In practice, a larger surface roughness factor corresponds to more turbulent filling process. The final inclusion volume for this case is 2.76 cm³, which is exactly ten times the value from Case 1. This is not surprising; looking at Equations (4) and (10), one sees that the growth rate of the inclusions is directly proportional to f_{sr}. This increased growth rate increases both the maximum and average inclusion diameters. The diameter of the largest inclusion is about 7.8 mm in Case 5, as opposed to 2.7 mm in Case 1. The final number of inclusions increases from 146,522 in Case 1 to 196,058 in Case 5 (Table 1). This difference is due to a combination of two effects: the larger free surface area in Case 5 results in many more inclusions being generated (563,710 in Case 5 versus 212,604 in Case 1), even though the nucleation spacing is the same in both cases; on the other hand, the much larger size of the inclusions causes many more agglomerations in Case 5 compared to Case 1. Comparing Figures 10a and 14a, the peak inclusion fraction decreases almost in half, but the visible distribution in Figure 14a extends for almost 1000 microns, rather than for almost 500 microns as in Figure 10a (note the difference in the x-axis scales). Comparing Figures 10b and 14b, the volume distribution in Case 5 is spread over a much wider range of diameters, and there are more large inclusions. One would not expect the distributions in Cases 1 and 5 to be similar, since the two cases correspond to much different physical situations.

An interesting overall observation from this study is that simulations with the same growth rate (Cases 1 − 4) all produce about the same total volume of inclusions. Furthermore, the size and volume distributions in Cases 1 − 3 are similar when normalized with the total final number of inclusions. As mentioned when discussing Figures 8 and 9a, the inclusion simulation results at the end of filling for all five cases looked qualitatively very similar (i.e., the largest inclusions ended up in roughly the same location). It is encouraging to see similar results from the model as relatively arbitrary parameters such as nucleation spacing and grid size are varied. Of course, the final inclusion sizes depend strongly on whether the inclusions are modeled as spheres or as disks, the roughness of the free surface during filling, and the oxidation rate.

4. Ongoing Work

While the present inclusion model is showing promising results, there are still enhancements to be made. The primary area of enhancement is to implement an improved oxidation rate model, such that the mass transfer coefficient, β, is a function of the local flow conditions. A similar improvement will be made with respect to the surface roughness factor. Additional simulations will be performed to test the inclusion release model, in order to examine the effect of the cleanliness of the melt entering the mold from the ladle. Most importantly, more comparisons with casting trials are needed. In particular, differences in the prediction of reoxidation inclusions due to changes in the pouring practice or the gating system and mold design need to be compared with measurements performed on actual steel castings.

Acknowledgements

References

[1] J.M. Svoboda, R.W. Monroe, C.E. Bates and J. Griffin (1987), "Appearance and Composition of Oxide Macroinclusions in Steel Castings," *AFS Transactions*, Vol. 95, pp. 187-202.

[2] J.A Griffin and C.E. Bates (1991), "Ladle Treating, Pouring and Gating for the Production of Clean Steel Castings," Steel Founders' Society of America Research Report No. 104.

[3] *MAGMASOFT*, MAGMA GmbH, Kackerstrasse 11, 52072 Aachen, Germany.

[4] Y. Wang, S. Shridhar, A.W. Cramb, A. Gomez and C. Cicutti (2004), "Reoxidation of Low-Carbon, Aluminum-Killed Steel," *AIST Transactions (Iron & Steel Technology)*, February 2004, pp. 87-96.

[5] Shibata, Yin and Emi (1998), "The Capillary Effect Promoting Collision and Agglomeration of Inclusion Particles at the Inert Gas-Steel Interface," *Phil. Trans. R. Soc. Lond. A*, Vol. 356, pp. 957-966.

Table 1.   Parameters and results for inclusion simulations.

Case	inclusion spacing l_0 (cm) at birth	number of metal cells	surface roughness factor f_{sr}	sphere /disk	number of inclusions generated	final number of inclusions	total inclusion volume (cm^3)	d_{max} (cm)	d_{avg} (cm)	t_{max} (cm)
1	0.5	26,053	1	S	212,604	146,522	0.276	0.269	0.0115	--
2	0.25	26,053	1	S	405,824	283,571	0.276	0.227	0.0091	--
3	0.25	13,263	1	S	302,876	219,285	0.279	0.210	0.0095	--
4	0.5	26,053	1	D	213,532	134,662	0.276	0.922	--	0.0237
5	0.5	26,053	10	S	563,710	196,058	2.76	0.782	0.0157	--
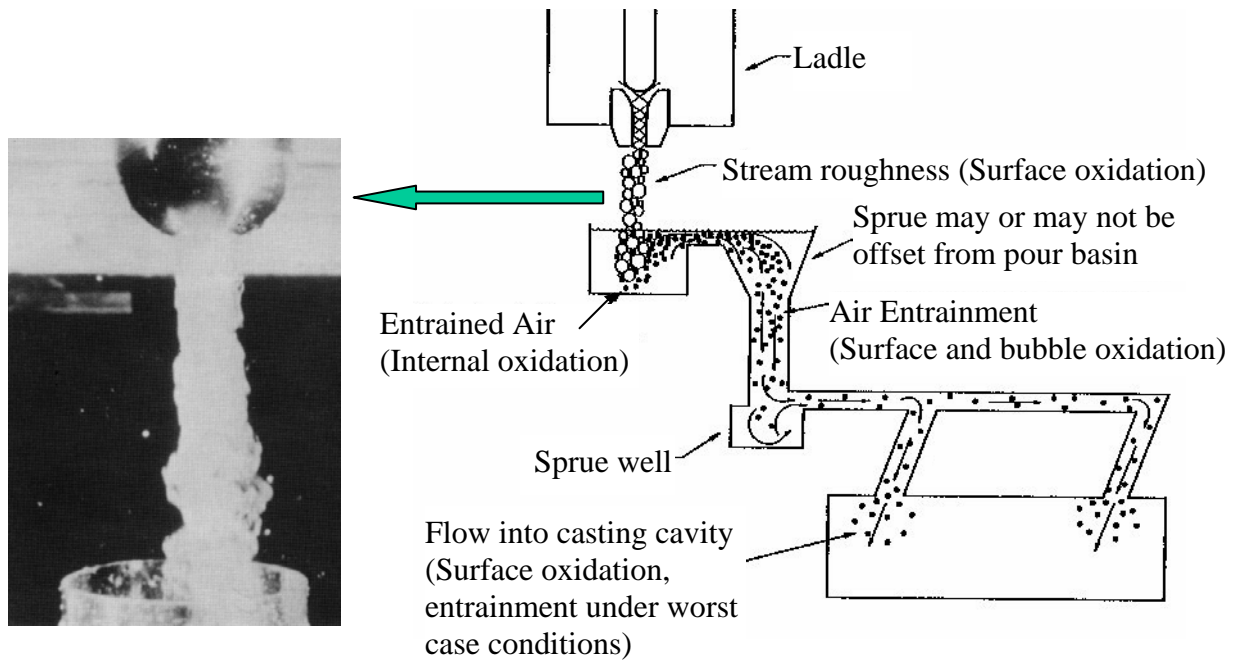
Figure 1. Opportunities for oxygen absorption during mold filling. Adapted from SFSA research report.[2]
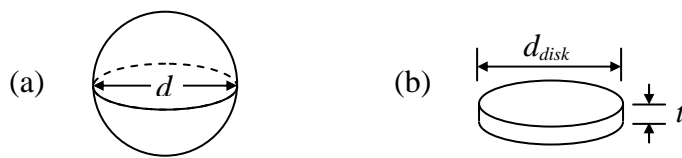
Figure 2. Possible inclusion geometries: (a) sphere; and (b) thin disk.
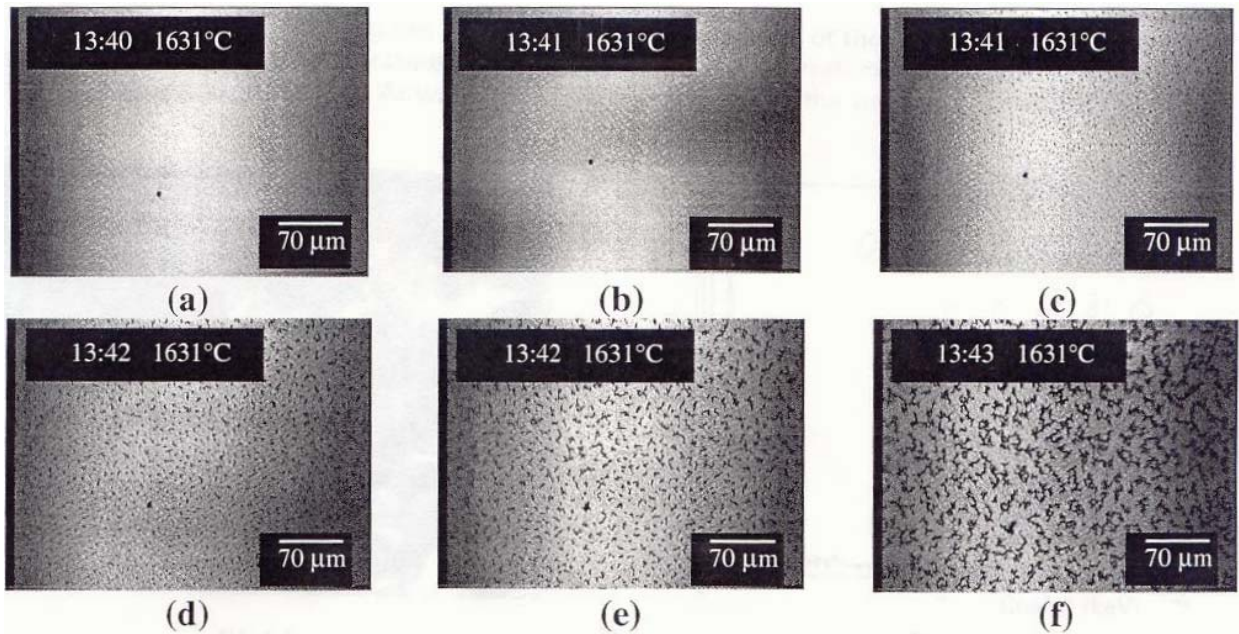
Figure 3.   Time-elapsed photographs of nucleation, growth and agglomeration of inclusions on a liquid steel free surface. Adapted from Wang et al.[4]
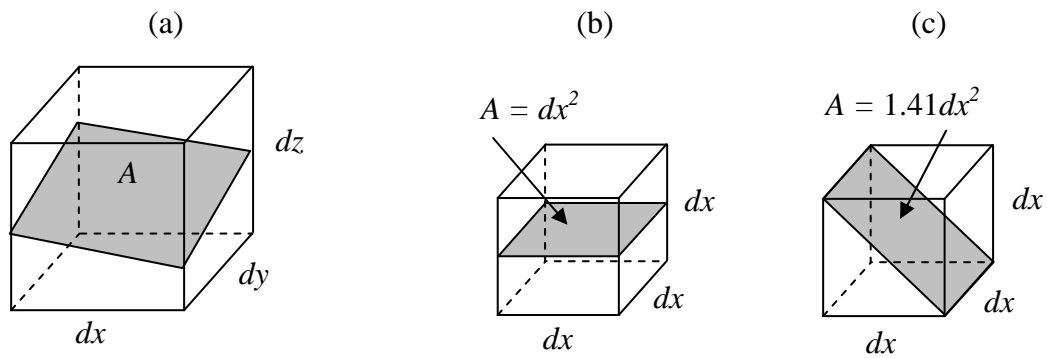
Figure 4.   Schematics showing the free surface area for a cell that is half-full of liquid metal: (a) general surface; (b) minimum surface area; and (c) maximum surface area.
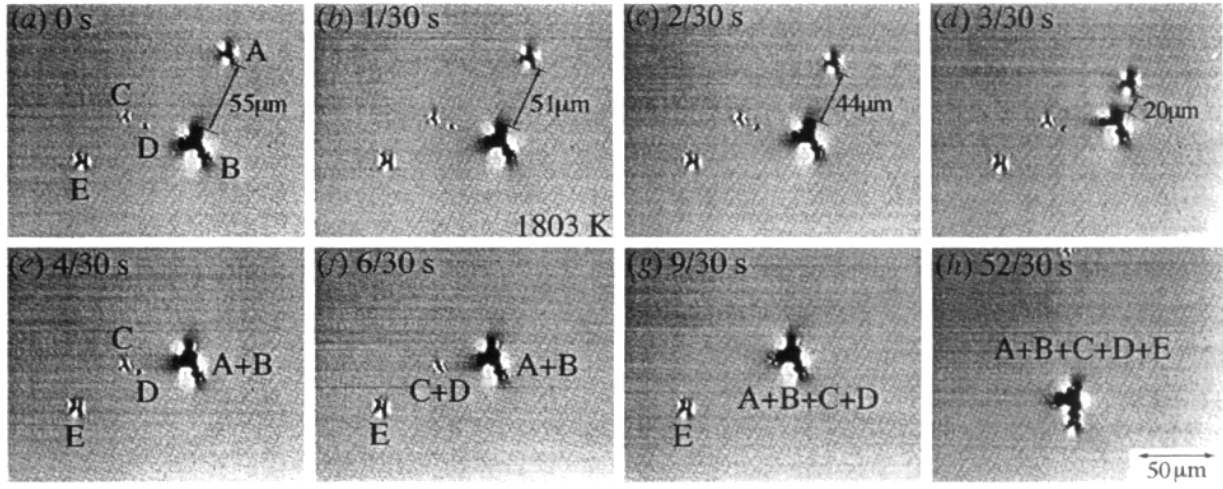
Figure 5. Time-elapsed photographs of inclusions agglomerating on the surface of liquid steel. Adapted from Shibata et al.[5]
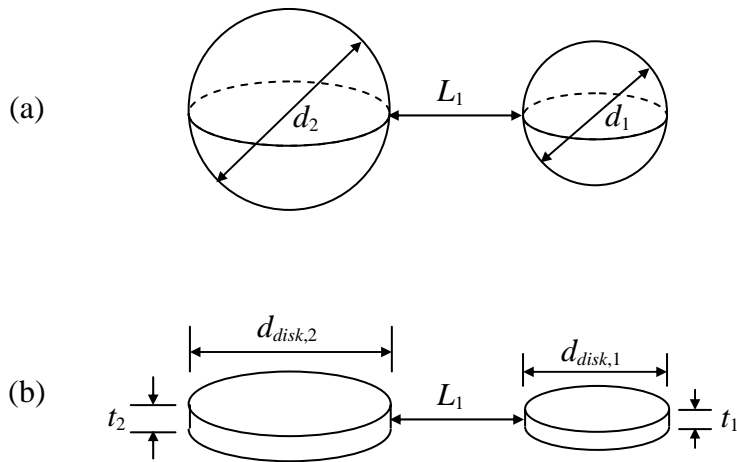
Figure 6. Schematics showing the critical distance, L_1, for the agglomeration of (a) spheres; and (b) disks.
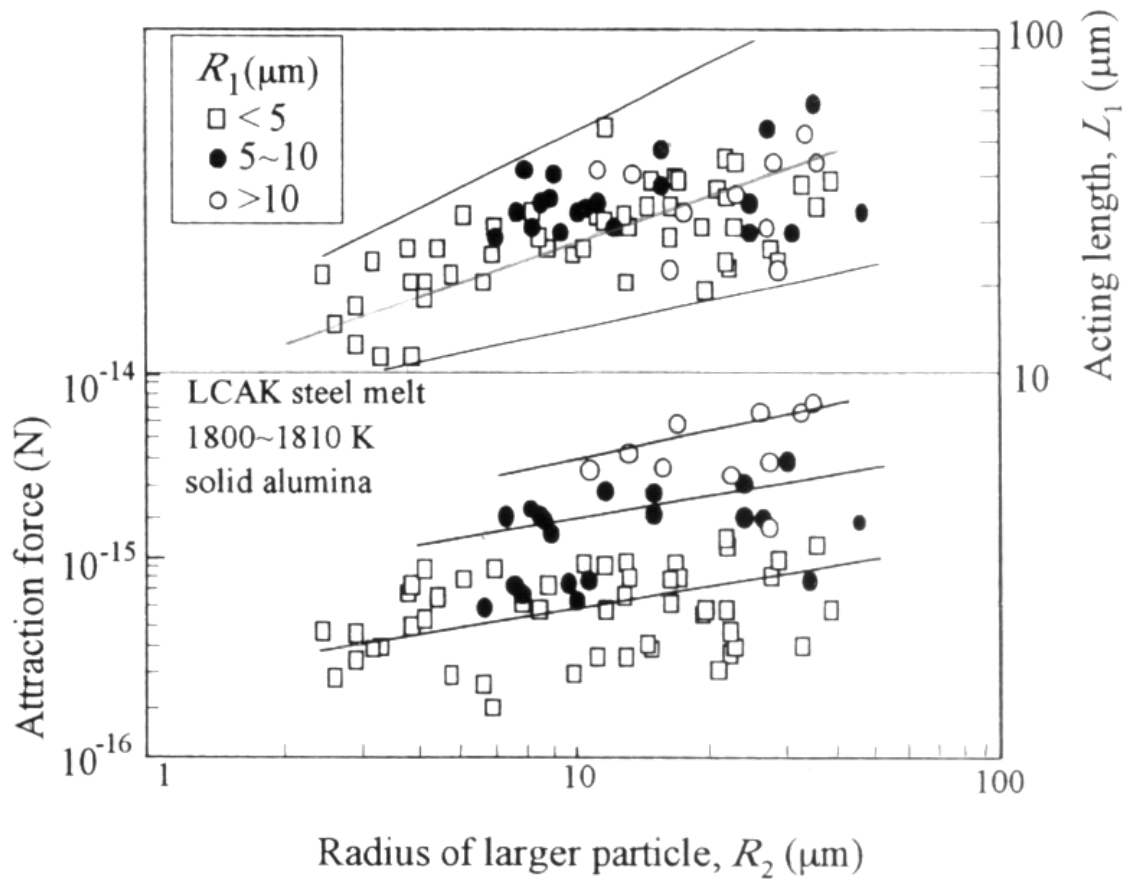
Figure 7.   Experimental agglomeration data, showing relations between inclusion radii and the attraction force and acting length (critical distance L_1). R_1 is the radius of the smaller inclusion, and R_2 is the radius of the larger inclusion. Adapted from Shibata et al.[5]
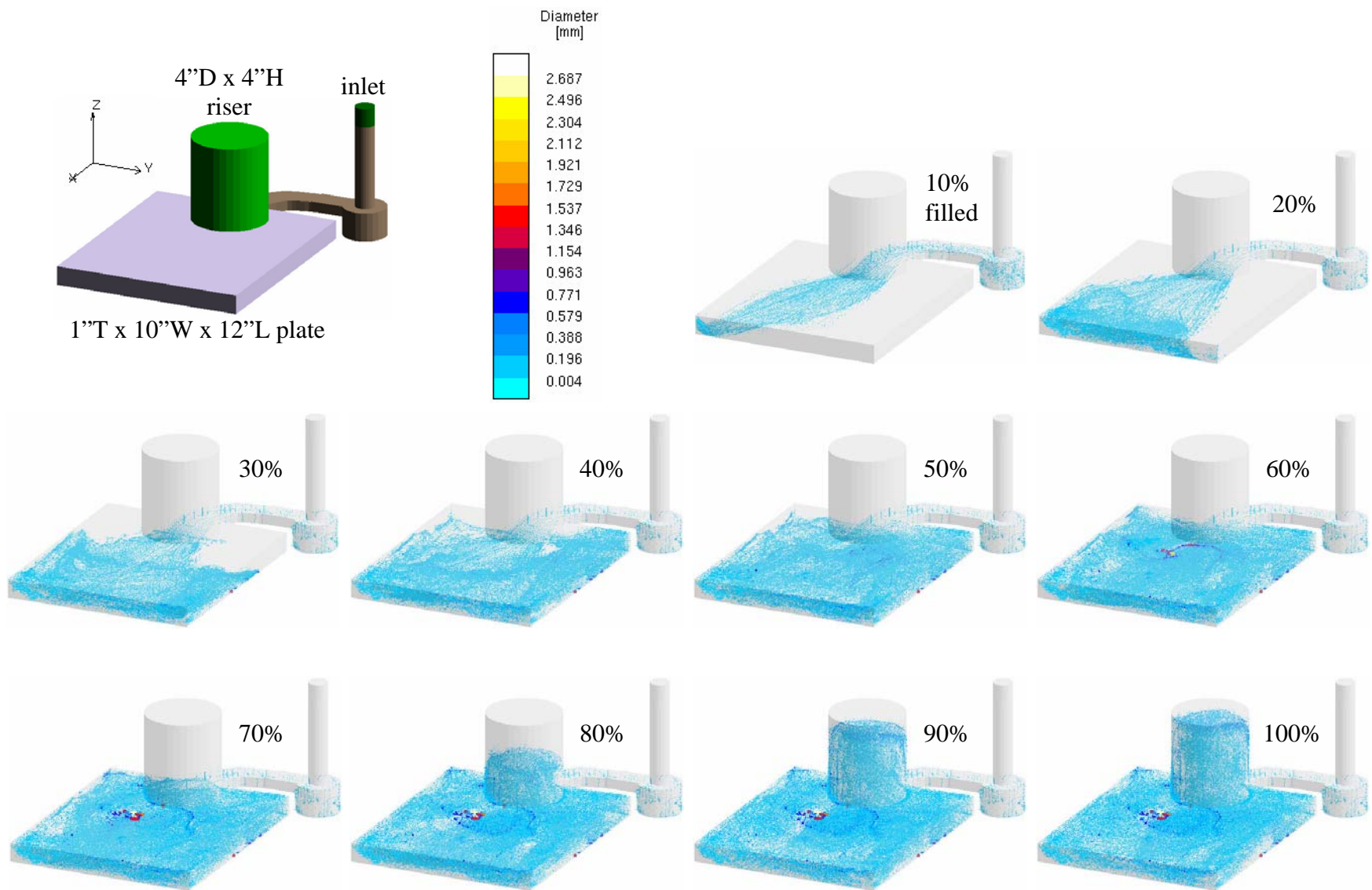
Figure 8.   Simulated inclusions at various times during filling for Case 1. Inclusions shown at 3x magnification.

(a)

(b)
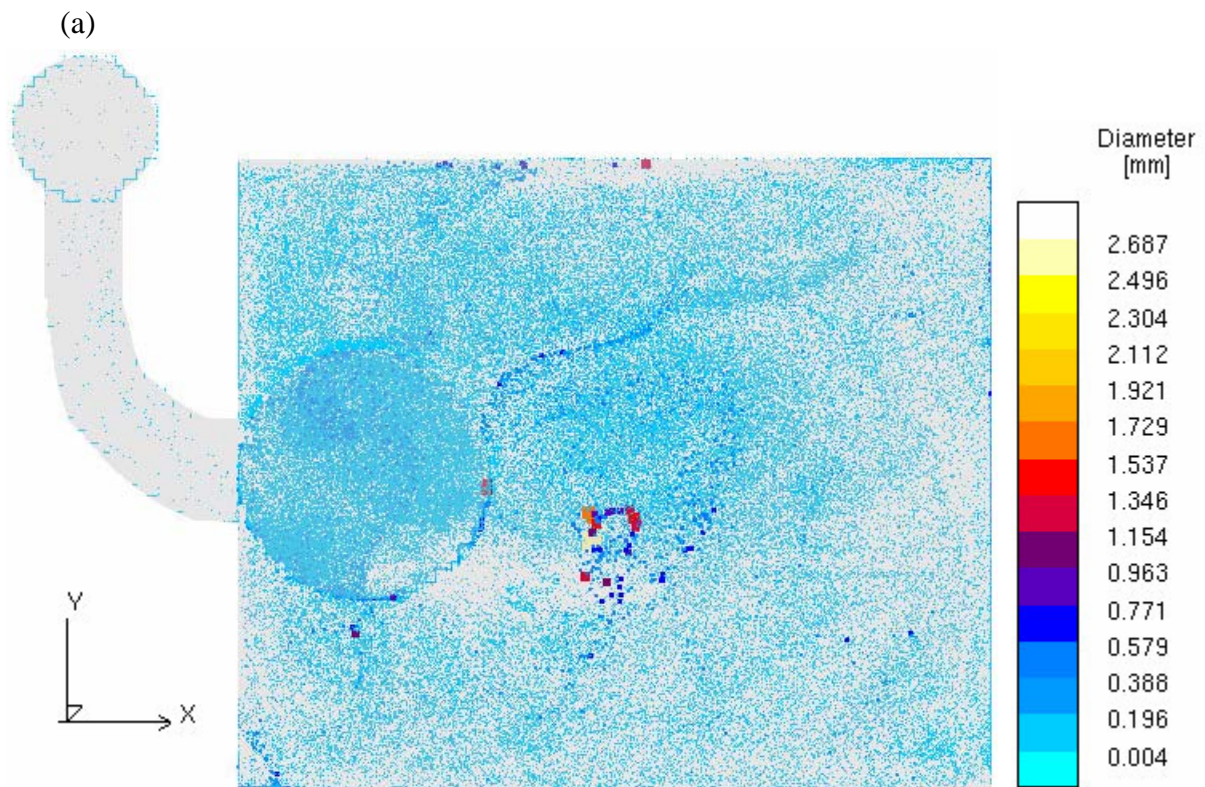
Figure 9.   Comparison between simulation and experimental results: (a) Top view of final simulated inclusion locations.   Inclusions shown at 3x magnification; (b) photo showing inclusion locations on the cope surface of two experimental plates.

(a)

$d_{max} = 2687$ μm

Fraction Of Inclusions Per Micron (μm^{-1})

Inclusion Diameter (μm)

(b)

$d_{max} = 2687$ μm

Inclusion Volume Fraction Per Micron (μm^{-1})
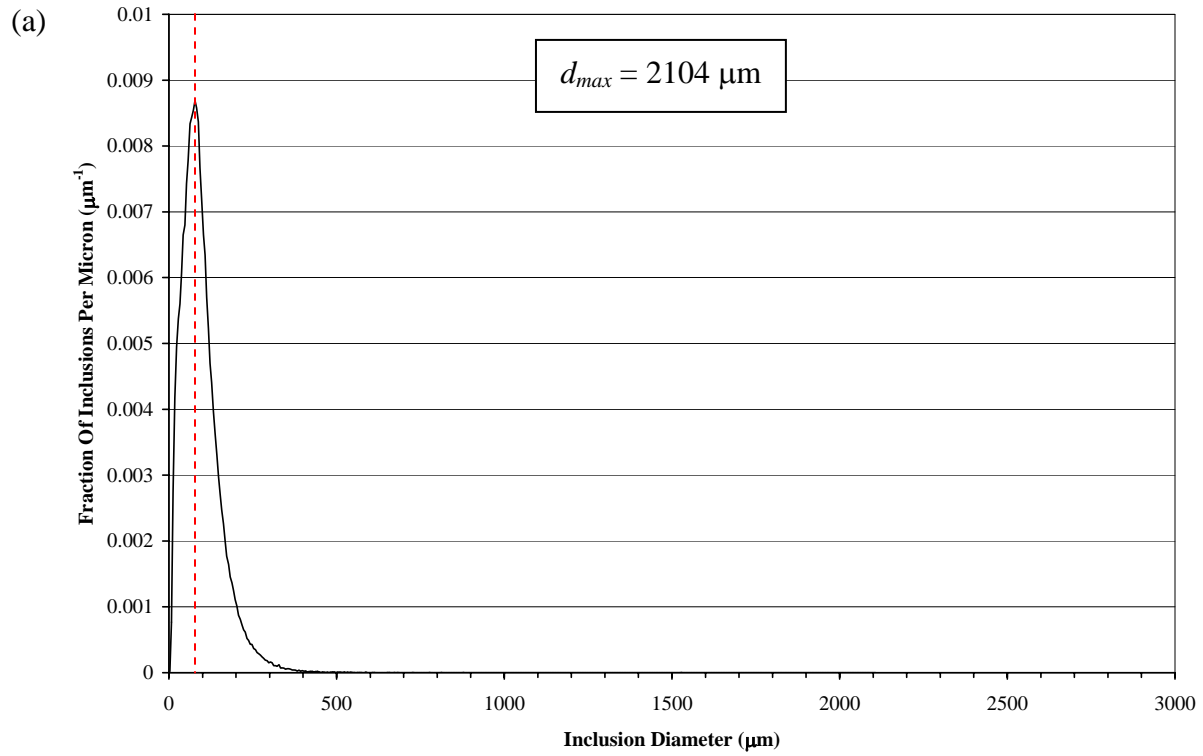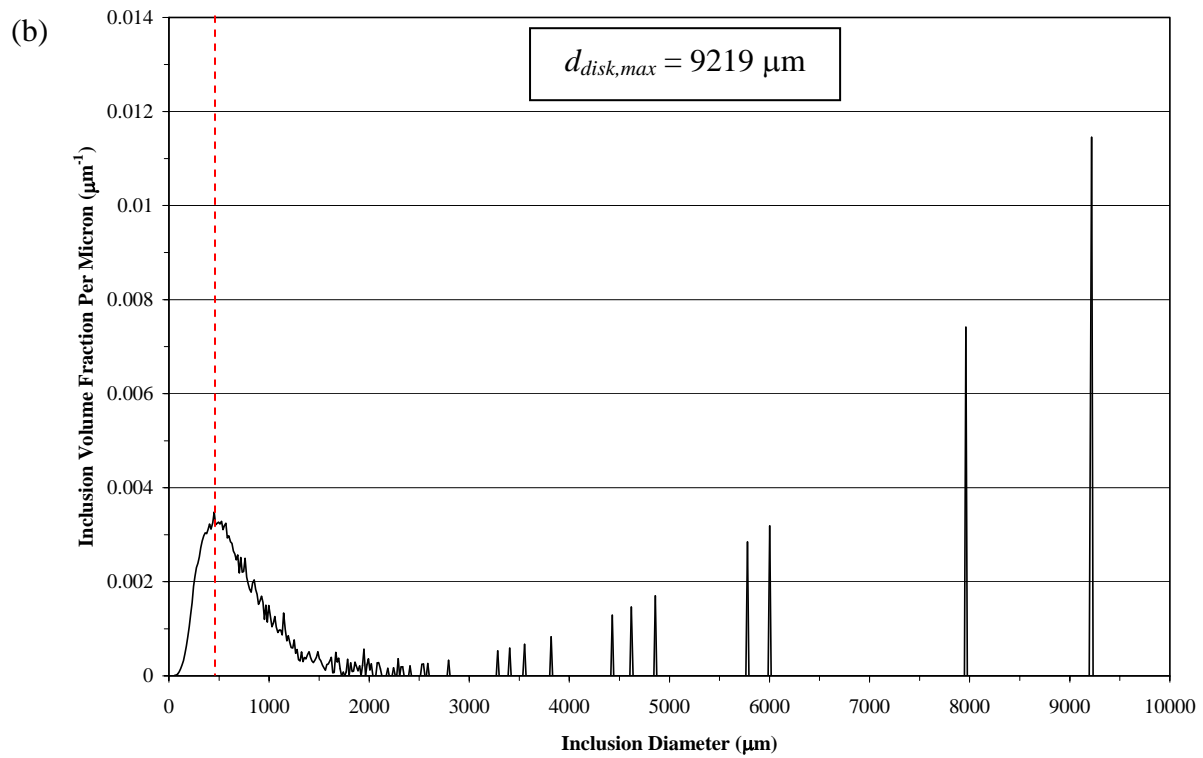
Inclusion Diameter (μm)
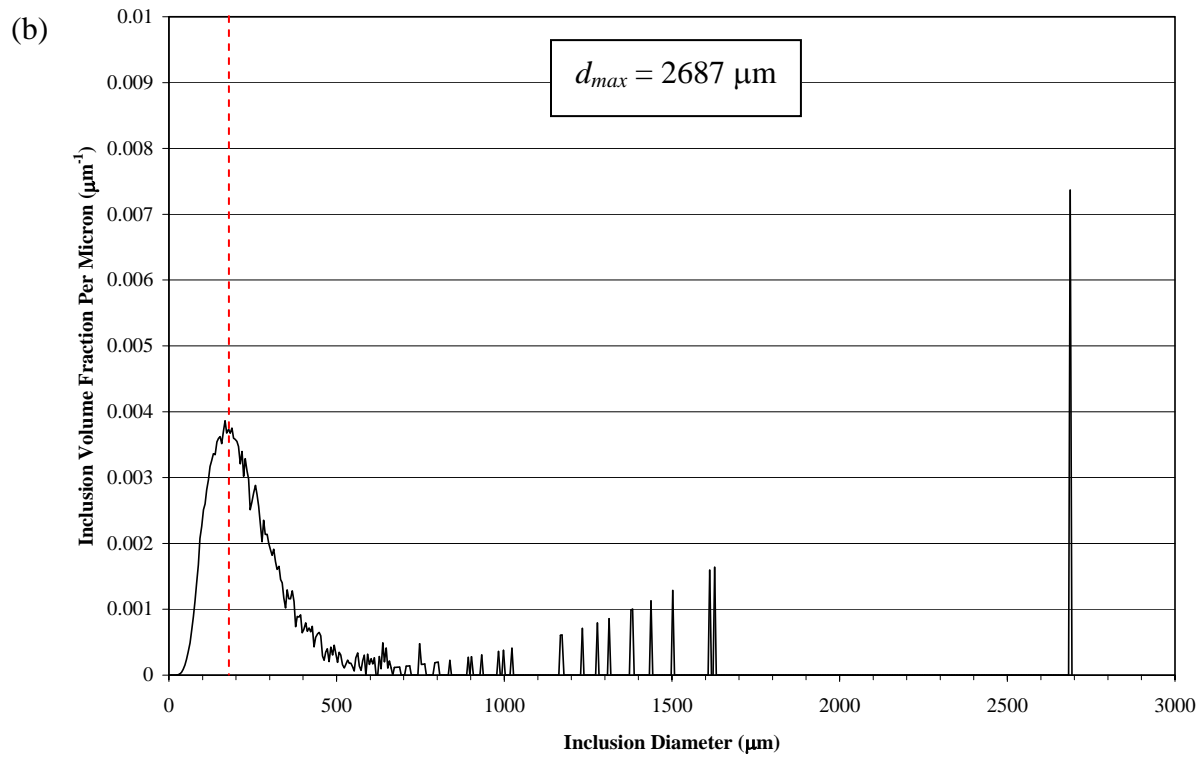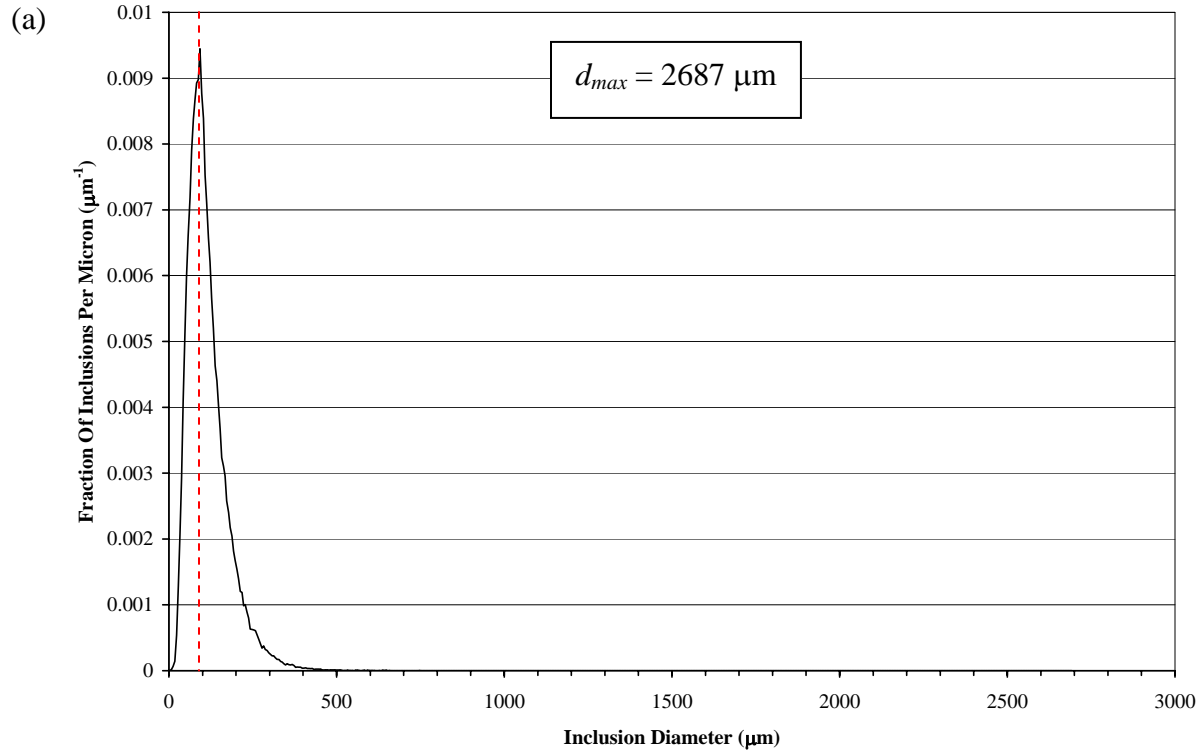
Figure 10.   Distribution of (a) number of inclusions based on diameter; and (b) inclusion volume based on diameter for Case 1.

(a)

(b)
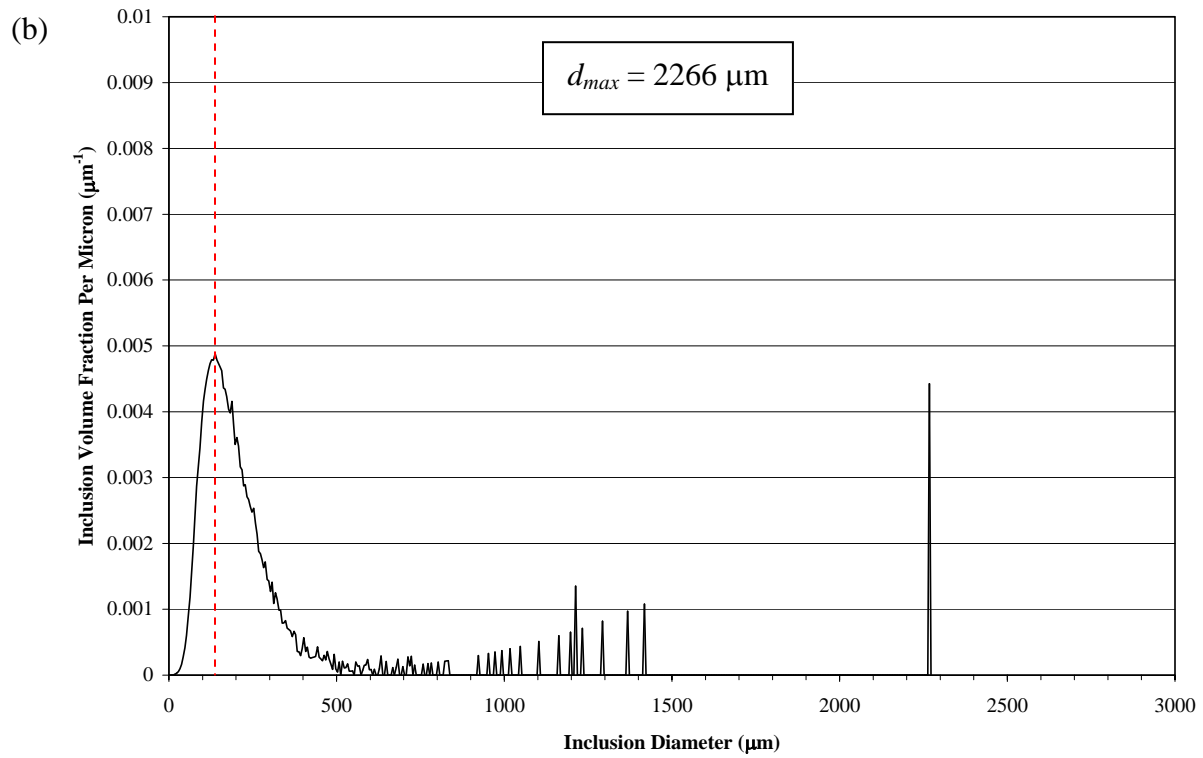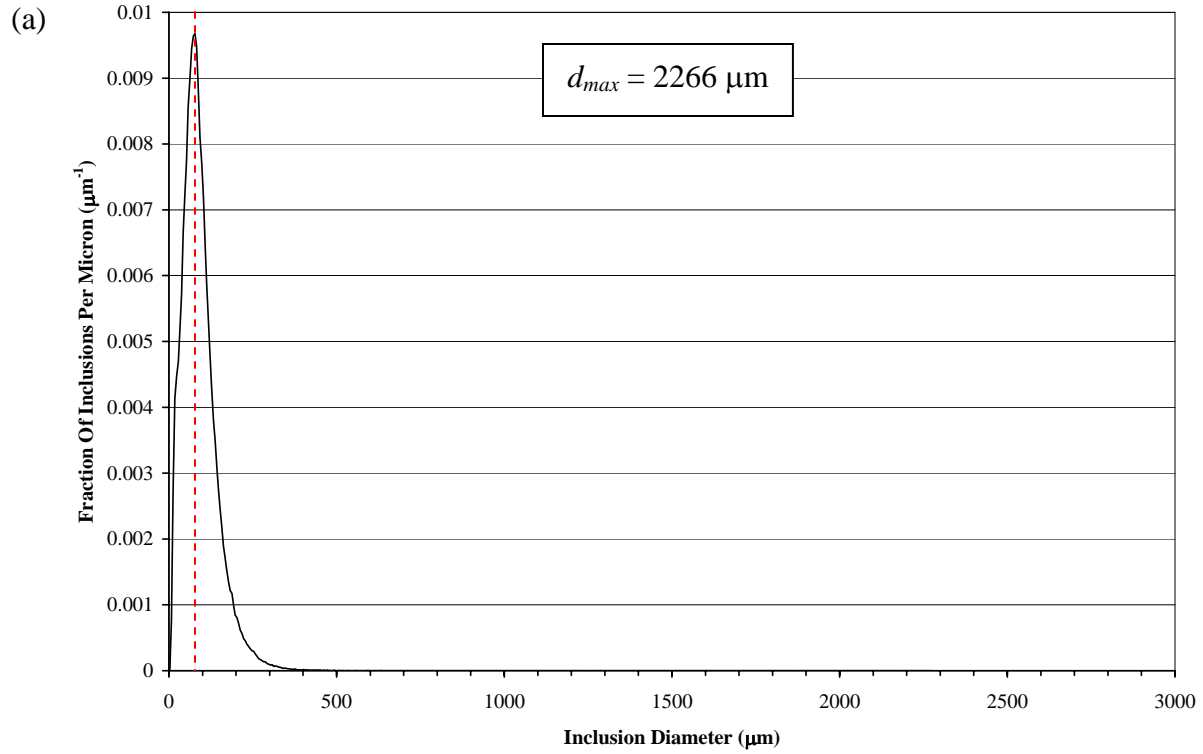
Figure 11. Distribution of (a) number of inclusions based on diameter; and (b) inclusion volume based on diameter for Case 2.
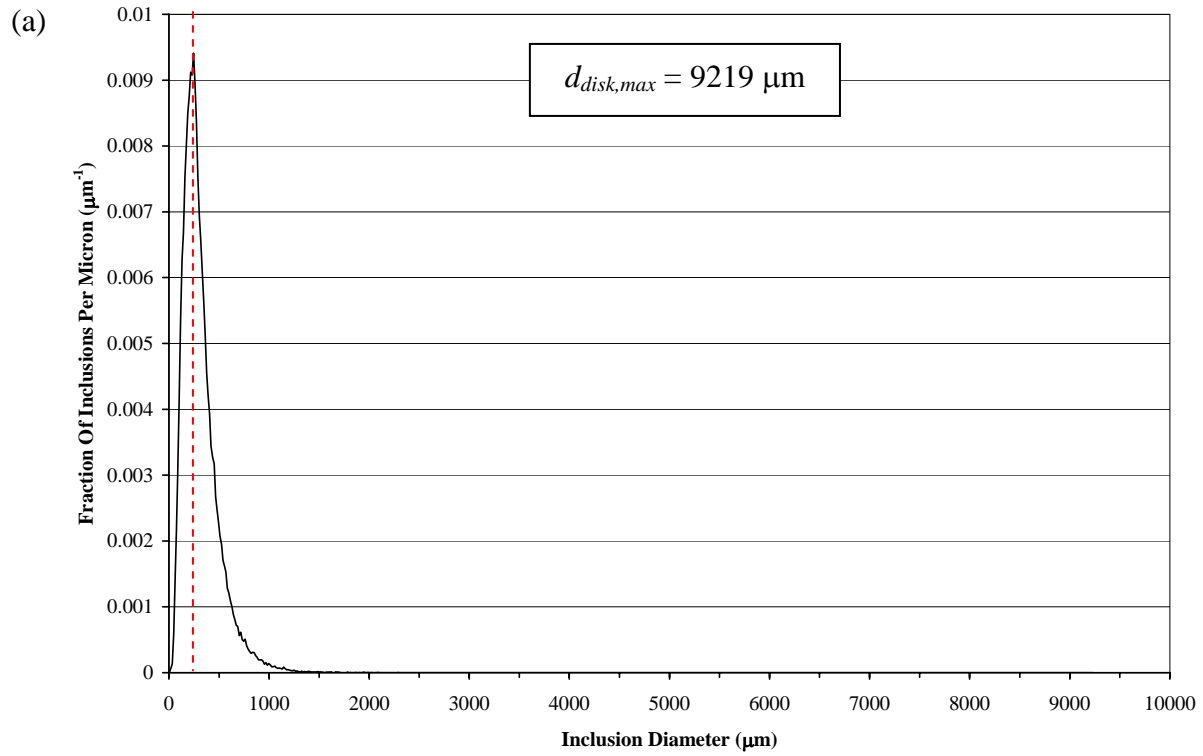
(a)

$d_{max} = 2104$ μm

(b)

$d_{max} = 2104$ μm
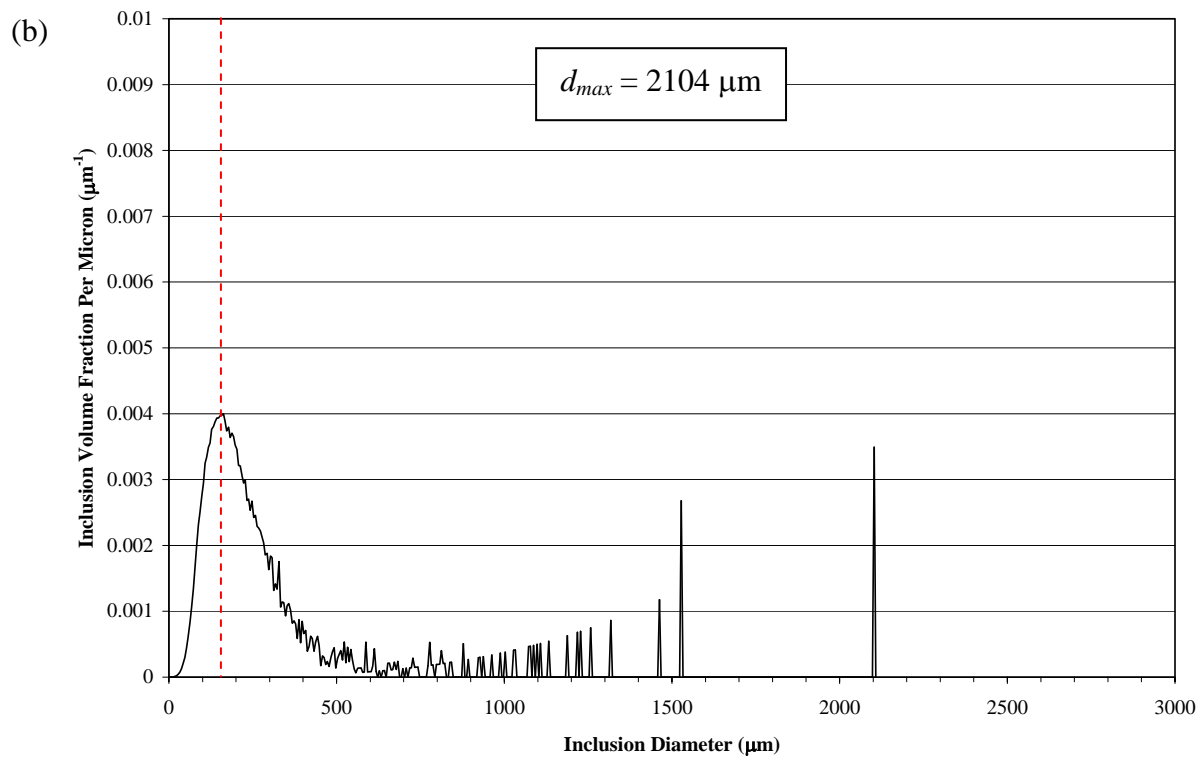
Figure 12. Distribution of (a) number of inclusions based on diameter; and (b) inclusion volume based on diameter for Case 3.

Figure 13. Distribution of (a) number of inclusions based on diameter; and (b) inclusion volume based on diameter for Case 4.
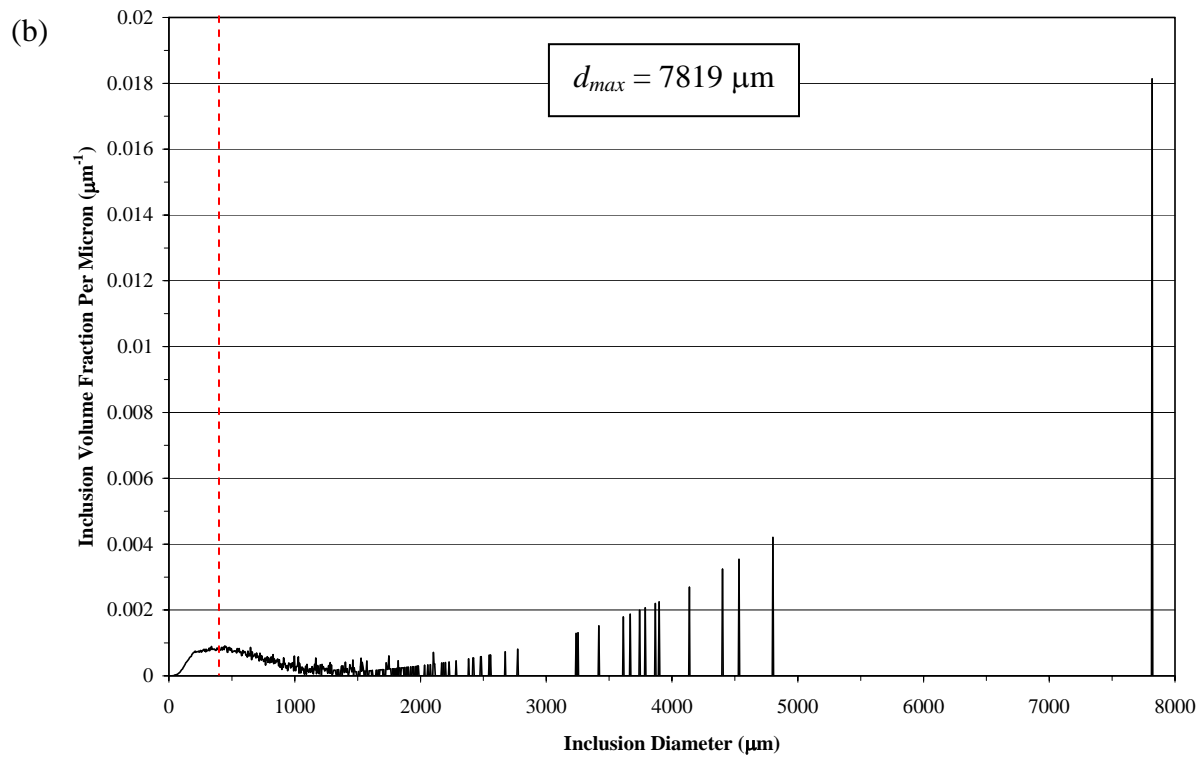
(a)

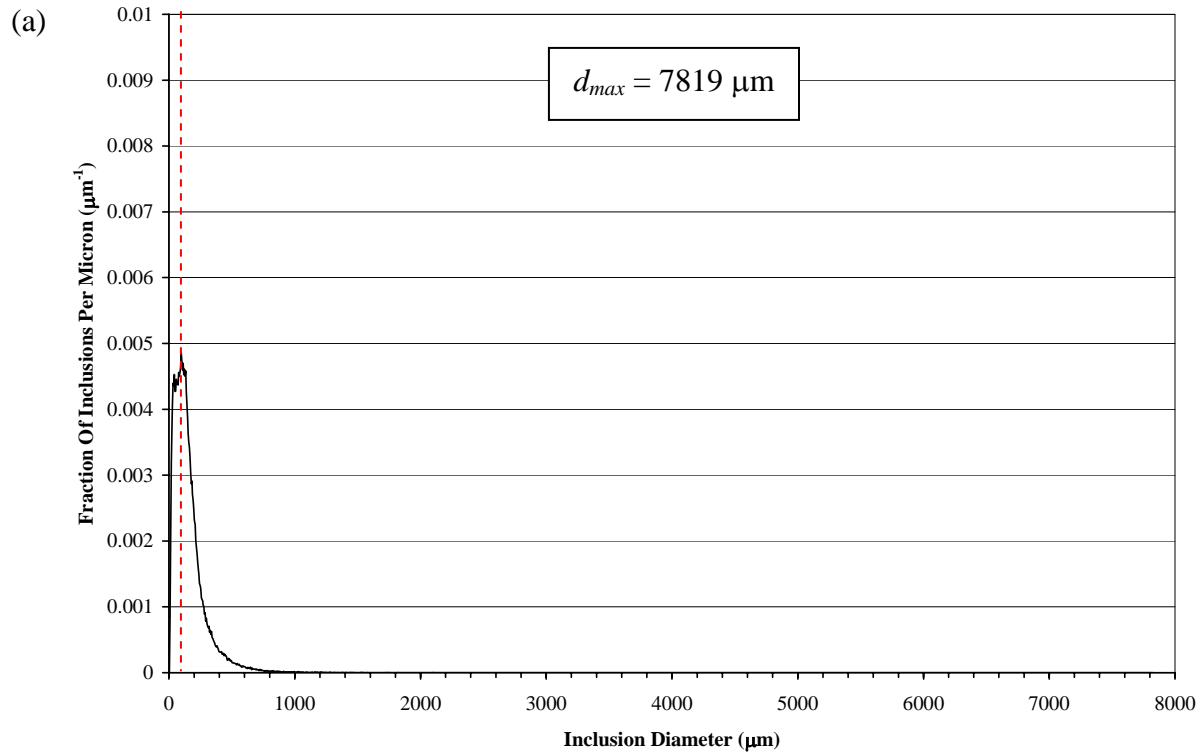$d_{max} = 7819$ μm

(b)

$d_{max} = 7819$ μm

Figure 14. Distribution of (a) number of inclusions based on diameter; and (b) inclusion volume based on diameter for Case 5.